



An Absolute Mass, Precise Age, and Hints of Planetary Winds for WASP-121A and b from a JWST NIRSpec Phase Curve

David K. Sing^{1,2} , Thomas M. Evans-Soma^{3,4} , Zafar Rustamkulov¹ , Joshua D. Lothringer⁵ , Nathan J. Mayne⁶ , and Kevin C. Schlaufman² 

¹ Department of Earth & Planetary Sciences, Johns Hopkins University, Baltimore, MD, USA; dsing@jhu.edu

² William H. Miller III Department of Physics & Astronomy, Johns Hopkins University, 3400 N Charles St, Baltimore, MD, USA

³ School of Information and Physical Sciences, University of Newcastle, Callaghan, NSW, Australia

⁴ Max Planck Institute for Astronomy, Königstuhl 17, D-69117 Heidelberg, Germany

⁵ Space Telescope Science Institute, Baltimore, MD 21218, USA

⁶ Department of Physics and Astronomy, Faculty of Environment Science and Economy, University of Exeter, EX4 4QL, UK

Received 2024 July 22; revised 2024 September 17; accepted 2024 September 22; published 2024 November 1

Abstract

We have conducted a planetary radial velocity measurement of the ultrahot Jupiter WASP-121b using JWST NIRSpec phase curve data. Our analysis reveals the Doppler shift of the planetary spectral lines across the full orbit, which shifts considerably across the detector (~ 10 pixels). Using cross-correlation techniques, we have determined an overall planetary velocity amplitude of $K_p = 215.7 \pm 1.1 \text{ km s}^{-1}$, which is in good agreement with the expected value. We have also calculated the dynamical mass for both components of the system by treating it as an eclipsing double-line spectroscopic binary, with WASP-121A having a mass of $M_* = 1.330 \pm 0.019 M_\odot$, while WASP-121b has a mass of $M_p = 1.170 \pm 0.043 M_{\text{Jup}}$. These dynamical measurements are $\sim 3\times$ more precise than previous estimates and do not rely on any stellar modeling assumptions that have a $\sim 5\%$ systematic floor mass uncertainty. Additionally, we used stellar evolution modeling constrained with a stellar density and parallax measurement to determine a precise age for the system, found to be $1.11 \pm 0.14 \text{ Gyr}$. Finally, we observed potential velocity differences between the two NIRSpec detectors, with NRS1 lower by $5.5 \pm 2.2 \text{ km s}^{-1}$. We suggest that differences can arise from day/night asymmetries in the thermal emission, which can lead to a sensitivity bias favoring the illuminated side of the planet, with planetary rotation and winds both acting to lower a measured K_p . The planet's rotation can account for 1 km s^{-1} of the observed velocity difference, with $4.5 \pm 2.2 \text{ km s}^{-1}$ potentially attributable to vertical differences in wind speeds.

Unified Astronomy Thesaurus concepts: Radial velocity (1332); Extrasolar gaseous planets (2172); Astronomical techniques (1684)

Materials only available in the online version of record: data behind figures

1. Introduction

For transiting exoplanets, estimates of the stellar mass have predominantly relied on stellar evolution models constrained by measurements, including parallax, stellar radial velocity (RV), and stellar density (J. D. Hartman et al. 2019; C. Hellier et al. 2019; S. W. Yee et al. 2023). Alternatively, a planet's RV signal can also be used, and high-resolution ground-based infrared spectrographs have been used to detect exoplanet molecular features over the last decade, beginning with I. A. G. Snellen et al. (2010), who used the CO lines to constrain the absolute stellar mass as the planetary Doppler shift was measured. As ground-based spectrographs have large systematics from sources such as telluric contamination and are limited in the uninterrupted duration they can observe, it is challenging to capture a complete phase curve of an exoplanet from the ground (see the review by J. L. Birkby 2018 for additional details). Most such observations to date have concentrated around the transit or eclipse phase to measure the planet's spectrum, which is not an optimal phase to measure the planet's radial-velocity semiamplitude and thus is not ideal for precision stellar mass measurements. However, some

measurements do cover larger phase ranges (typically between phases 0.3 and 0.7), such as L. van Sluijs et al. (2023), who covered WASP-33 b, or A. Ridden-Harper et al. (2023), who measured KELT-9 b. These observations typically cover phase ranges between ~ 0.3 and 0.75 , resulting in precise ($\sim 0.5\%$) planetary semiamplitudes.

JWST has enabled detailed spectral measurements of transiting exoplanets using transmission, emission, and phase curve spectroscopy (e.g., Z. Rustamkulov et al. 2022; P. C. August et al. 2023; J. L. Bean et al. 2023; T. Mikal-Evans et al. 2023; T. J. Bell et al. 2024). The infrared observatory has proven to be an extremely stable platform (N. Espinoza et al. 2023; J. Rigby et al. 2023) with achievable photometric precisions on the order of 10 s of parts per million or better (e.g., L.-P. Coulombe et al. 2023; J. Lustig-Yaeger et al. 2023). The NIRSpec G395H grating, in particular, has shown to be extremely sensitive to the strong molecular absorption from CO₂ (JWST Transiting Exoplanet Community Early Release Science Team et al. 2023; Z. Rustamkulov et al. 2023) and CO (L. Alderson et al. 2023). As seen in the direct imaging planet VHS 1256-1257 b (B. E. Miles et al. 2023) and the transiting planet WASP-39b (D. Grant et al. 2023), the fundamental CO bandheads between 4.4 and $5 \mu\text{m}$ are resolvable with G395H. Cross-correlation techniques have also been shown to be capable of detecting CO with NIRSpec/G395H (E. Esparza-Borges et al. 2023). With CO resolvable in long-stare



Original content from this work may be used under the terms of the [Creative Commons Attribution 4.0 licence](https://creativecommons.org/licenses/by/4.0/). Any further distribution of this work must maintain attribution to the author(s) and the title of the work, journal citation and DOI.

complete phase-curve observations, JWST should be able to enable precision mass measurements if the planet’s Doppler shift can be detected. Moreover, as demonstrated by Z. Rustamkulov et al. (2023), the precise stellar densities derived from the high signal-to-noise JWST transit light curves enable very tight constraints on stellar evolution models.

WASP-121b is an ultrahot Jupiter that is particularly favorable for atmospheric measurements (L. Delrez et al. 2016). Various features have been detected in its atmosphere, including H₂O and Fe, through HST transmission, emission, and phase-curve measurements (T. M. Evans et al. 2016, 2017, 2018; T. Mikal-Evans et al. 2019, 2023; D. K. Sing et al. 2019). The planet has also been observed in optical transmission high-resolution spectra, with a large number of atomic species detected (M. Ben-Yami et al. 2020; V. Bourrier et al. 2020; S. H. C. Cabot et al. 2020; N. P. Gibson et al. 2020; F. Borsa et al. 2021; S. R. Merritt et al. 2021; T. Azevedo Silva et al. 2022; H. J. Hoeijmakers et al. 2024; C. Maguire et al. 2023; J. V. Seidel et al. 2023; J. P. Wardenier et al. 2024). Notably, the planet velocities measured from ESPRESSO transit measurements range from 197 to 213 km s⁻¹ (C. Maguire et al. 2023), which are significantly lower than the expected orbital velocity of the planet. Such a discrepancy could be a signature of winds or atmospheric escape. In addition, J. P. Wardenier et al. (2024) found phase-dependent Doppler shifts in CO and H₂O around transit, due to a combination of planetary rotation and the spatial distribution of the molecular species.

In this work, we present new planetary RV measurements of WASP-121b using the JWST/NIRSpec G395H instrument, which has a spectral resolution near $R \sim 3000$. This resolution is sufficient to observe significant wavelength shifts across the detector for short-period planets, given the large orbital velocities near ~ 200 km s⁻¹ compared to the NRS1 and NRS2 detector’s average resolutions of 67 and 44 km s⁻¹ per pixel, respectively. We note for JWST the NIRSpec high-resolution gratings will be needed for studies of this nature. For instance, with resolutions near 700 for NIRISS SOSS, the planet would only move across a couple of pixels peak-to-peak during the orbit, making it difficult to remove the stellar contribution cleanly. We describe the data reduction in Section 2, our analysis in Section 3, present our methods in Section 4, give results in Section 5, and conclude in Section 6.

2. Data Reduction

We use the phase-curve measurements of WASP-121b taken with the JWST NIRSpec G395H instrument as part of GO-1729 (P.I. Mikal-Evans, co-P.I. Kataria). The data continuously cover the entire phase curve of the planet lasting 1.57 days, beginning just before secondary eclipse and ending shortly after a second secondary eclipse (see Figure 1). The NIRSpec/G395H grating covers wavelengths from $\lambda = 2.70$ to $5.15 \mu\text{m}$ at a resolution of $R \sim 3000$.

This data set and the reductions used here have been described in T. Mikal-Evans et al. (2023). In short, we use the FIREFLY suite to reduce the JWST data starting from the uncalibrated data (Z. Rustamkulov et al. 2022, 2023), optimizing the JWST calibration pipeline for time series observations. The customized routines include removal of $1/f$ noise at the group and integration level, bad pixel removal, cosmic-ray cleaning spatially, and an optimized extraction of the stellar spectrum.

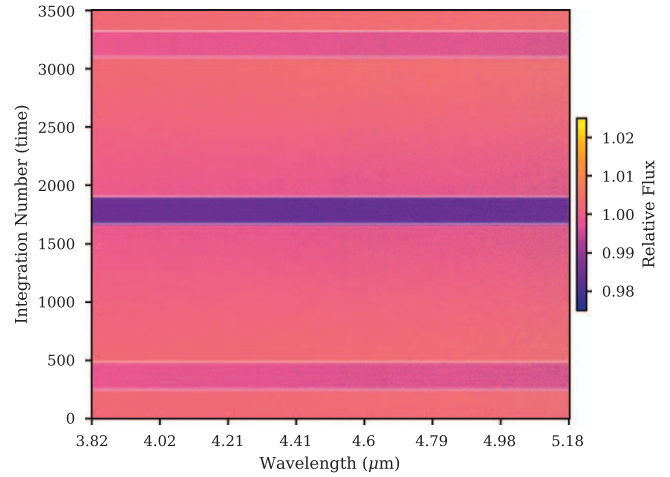


Figure 1. NIRSpec G395H NRS2 spectrophotometry. Plotted is the WASP-121 spectra vs. detector integration number, which is proportional to time, with the color bar corresponding to the normalized flux. The transit can clearly be seen in the middle as well as the two eclipses at the top and bottom of the plot. The beginning and end of the transits and eclipses are marked with white horizontal lines.

From the extracted time series spectra (TSS), we removed stellar flux and planetary continuum flux from the data using the following procedure to isolate the planetary emission/absorption lines. For each integration we did as follows:

1. Removed the white-light phase-curve contribution from each TSS, dividing the spectrophotometric time series at each wavelength by the wavelength-integrated white-light curve.
2. Divided out the median spectra of the whole time series from each TSS. This procedure removes the stellar flux contribution and a portion of the planetary continuum while preserving the Doppler-shifting planetary spectral lines. We note the Doppler shift of the stellar lines is well below the instrument resolution, so the stellar lines are assumed to be stable throughout the phase-curve observation.
3. Removed the phase-dependent planet continuum emission by dividing each TSS by a running median filter in the wavelength chosen to be 101 pixels wide. This procedure removes any remaining phase-dependent planetary continuum flux while preserving individual spectral lines of the planet.

The residual spectrophotometry can be seen in Figure 2, which we use in our cross-correlation analysis.

3. Analysis

The residual data cube (with dimensions of time, λ , and flux) has the stellar contribution of the star effectively removed along with the planet’s continuum flux, while the planetary spectral lines have been largely unaffected (see Figure 2). We note that the high quality of the JWST data allowed for cross-correlation measurements at this stage without the need for further cleaning or removal of further systematic errors in the data. Such additional steps are typically needed for ground-based high-resolution spectroscopy to remove, for instance, telluric contamination, airmass trends, or detector drifts (e.g., J. L. Birkby et al. 2017). In addition, the JWST phase-curve

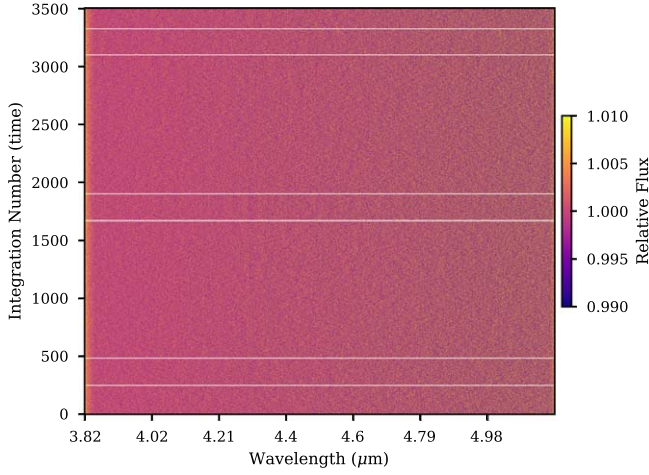


Figure 2. The same as Figure 1 but plotting the residual spectrophotometry after removing the median stellar spectra, white-light phase curve, and phase-dependent planetary broadband emission spectrum.

data is a single continuous observation, such that the full orbital velocity curve can be measured without night-to-night or visit-to-visit calibration differences.

The wavelength calibration for JWST NIRSpec has been found to meet the requirement of 1/8 of a resolution element (T. Böker et al. 2023). However, the accuracies assume a well-centered point source, and the BOTS mode uses a wide slit, which can lead to wavelength calibration offsets if the target is not well centered. Using stellar H lines, we compared the stellar spectra to a phoenix model at the known system velocity and found a wavelength shift over the default pipeline solution of about 1 pixel. Thus, a measurement of the system velocity with this data set will have a large 1 pixel systematic uncertainty, which prohibits a precise measurement. However, the relative planet velocities are preserved as the target remained well placed in the slit (1/500 of a pixel, $\sim 0.1 \text{ km s}^{-1}$) during the entire 37.8 hr phase-curve observation (T. Mikal-Evans et al. 2023).

3.1. Planet Velocity Measurement

Assuming a circular orbit, the expected measured planet velocity, v_p , can be calculated from the stellar radius and transit-derived parameters using

$$v_p = \frac{2\pi(a/R_\star)R_\star}{P} \sin(i), \quad (1)$$

where a/R_\star is the semimajor axis to stellar radii, P is the period, and i the inclination. Using the values found in V. Bourrier et al. (2020), the expected planet velocity is calculated to be $220 \pm 4 \text{ km s}^{-1}$, with the majority of the uncertainty due to the stellar radius. The G395H resolution varies from $R = 2000$ to 3500 between 3 and $5 \mu\text{m}$, corresponding to velocity resolutions of $150\text{--}85 \text{ km s}^{-1}$ or $68\text{--}38 \text{ km s}^{-1}$ per pixel, respectively. Thus, peak to trough the planetary signal is expected to shift across 6.5 pixels at $3 \mu\text{m}$ and 11.6 pixels at $5 \mu\text{m}$. With a shift >1 pixel, the planetary Doppler shift is expected to be readily detectable, especially when coadding the signal of many spectral lines across the detector.

To facilitate velocity measurements, using a cubic spline interpolation we resampled the G395H residual data cube

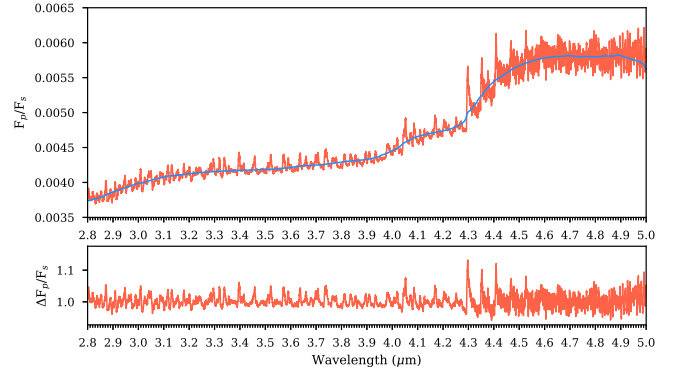


Figure 3. (Top) Phoenix forward model planetary spectrum corresponding to the dayside for WASP-121b. Emission lines from species such as CO are visible. (Bottom) The cross-correlation template Phoenix planetary spectrum generated by dividing by a median filter that removes the continuum emission.

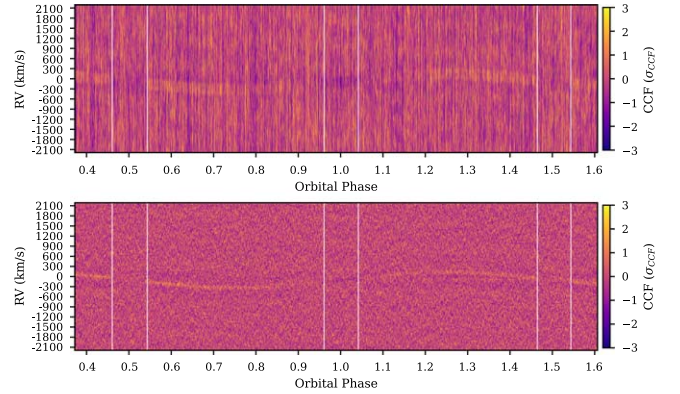


Figure 4. Cross-correlation amplitude as a function of orbital phase and RV lag using the Phoenix model as a correlation template. The CCF amplitude has been normalized at each phase by its standard deviation. (Top) Correlation using a Phoenix grid model as a correlation template. (Bottom) Using a PHOENIX model template derived from a retrieval on the planetary dayside emission spectra. Vertical white lines mark transit and eclipse first and fourth contact phases.

spectra on a uniform $\log(\lambda)$ wavelength scale and supersampled each pixel by a factor of 10. With the log resampling, the spectra have a corresponding constant resolution in velocity for each detector of 6.83 km s^{-1} per pixel for NRS1 and 4.45 km s^{-1} per pixel for NRS2.

3.1.1. Cross Correlation with Forward Models

We cross-correlated the resampled residual spectral data with a PHOENIX model (J. D. Lothringer et al. 2018) representative of the dayside spectrum (see Figure 3). The first model was an “out-of-the-box” forward model generated from a grid, while the second was the best-fit emission spectra from a retrieval fit to the G395H dayside emission spectra (Mikal-Evans et al. 2024, in preparation, private communication). Cross-correlation templates from the PHOENIX spectra were generated by removing the continuum with a median filter in wavelength as done for the data. The model template spectra have spectral emission features from CO and H_2O , which are expected based on previous measurements (e.g., T. Mikal-Evans et al. 2019). We cross-correlated the model template with all 3504 spectra in the time series data. The time-dependent correlation results for both the “out-of-the-box” and retrieval model spectra can be seen in Figure 4, showing the correlation as a function of RV lag and orbital phase. A correlation is seen in the data detected

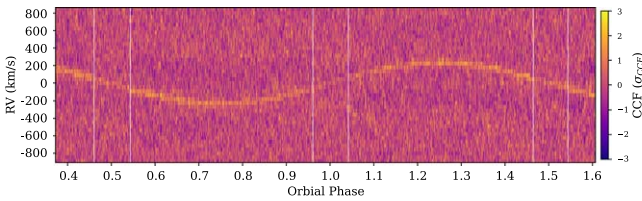


Figure 5. Same as Figure 4 but using a cross-correlation template derived from the data themselves.

at the phase and 220 km s^{-1} amplitude expected by the planetary velocity. For the “out-of-the-box” template spectra, a correlation can be seen, but the correlation peak itself is lower by a factor of 2 compared to the retrieval model, and the width of the cross-correlation function was found to be $3\text{--}4\times$ wider and notably flat-topped, prohibiting a precise velocity measurement. The dramatic difference between the model spectra highlights the sensitivity of cross-correlation techniques to the exact atmospheric model used and the difficulty of optimizing a signal if the atmospheric structure and composition are notably different than can be assumed from model grids. We note the cross-correlation function can be seen to flip to negative correlation values when correlating against the transit signal, as a transit spectrum has absorption lines that are darker in transit compared to the continuum, while inverted emission lines during secondary eclipse are brighter.

3.1.2. Self-derived Cross Correlation

Rather than use a planetary atmospheric model for the template spectra to correlate the data against, we also derived the template from the data themselves, as is commonly done when analyzing the RV signatures of binary stars (e.g., D. K. Sing et al. 2004). Using the planetary spectral features themselves as a template should, in principle, be fully optimal to measure relative velocity shifts as it avoids model mismatches including missing or incomplete cross sections and the assumed atmospheric structure and composition. However, with a self-derived template the absolute systemic velocity is not directly measured. In addition, residual stellar features and detector artifacts could be present in the empirical template, which might be picked up in the cross correlation at low levels near zero velocities.

We first velocity shifted all the spectra to the expected planetary rest frame assuming $K_p = 220 \text{ km s}^{-1}$, then computed the mean residual planetary spectrum of the entire residual time series. We then used the mean spectrum as a cross-correlation template, cross-correlating against the unshifted time series data. We normalized the cross-correlation signal strength by dividing the cross-correlation function (CCF) by its standard deviation. As seen in Figure 5, a planetary RV signal is evident when plotting the cross-correlation signal as a function of orbital phase, with the correlation peaks much better resolved than when using the forward model. In order to time-resolve the planet signal at each phase at a $2\text{--}3\sigma$ level, we binned the spectra in time by a factor of 16 (corresponding to 11.25 minute bins) and cross-correlated the binned spectra with our mean template. A Gaussian was then fit to the strongest cross-correlation peak to determine the peak velocity shift and its uncertainty at each phase. At a few phases, the peak cross-correlation signal did not correspond to a velocity near the expected planet velocity. Given it occurred for only a small number of phases, we implemented a 15σ clip to remove those

points. We additionally discarded the data during eclipse as the planetary emission is not observed during that time.

For both NRS1 and NRS2, we fit the RV curves with a sinusoid, fixing the period to that from V. Bourrier et al. (2020) and fitting for the amplitude K_p and the absolute velocity (see Figures 6 and 7). Additionally fitting for a phase shift did not improve the fit, so no offset was assumed. To search for nonsinusoidal components, we additionally tried fitting the RV data with a high-order polynomial chosen to be a Taylor expansion of a sinusoid but did not find statistically significant results as measured by the Bayesian information criteria. For NRS1, we measure a velocity of $K_p = 212.7 \pm 1.8 \text{ km s}^{-1}$ while $K_p = 218.2 \pm 1.3 \text{ km s}^{-1}$ for NRS2. Although NRS2 has less total flux than NRS1, we find slightly higher precisions for NRS2 likely due to larger planetary emission along with correlating against stronger, more favorable planetary features such as the comb-like CO lines. We report the weighted mean value of K_p in Table 2. The RV data are available on Zenodo (10.5281/zenodo.11992282).

4. Methods

4.1. Dynamical Mass Measurements

With the RV of the star and planet both measured along with the inclination, we derive the masses for both components using the following equation from G. Torres et al. (2010):

$$M_{(\star,p)} \sin^3(i) = 1.036149 \times 10^{-7} (1 - e^2)^{3/2} (K_\star + K_p)^2 K_{(p,\star)} P, \quad (2)$$

where $M_{(\star,p)}$ is the mass of the star or planet (depending on which is being calculated), K_\star is the stellar RV, and e is the eccentricity. Using K_\star from L. Delrez et al. (2016), both e and P from V. Bourrier et al. (2020), and a K_p value of $215.7 \pm 1.1 \text{ km s}^{-1}$ derived from our JWST data, we find a stellar mass of $M_\star = 1.330 \pm 0.019 M_\odot$ and $M_p = 1.170 \pm 0.043 M_J$. We note that these dynamical mass measurements are about as precise as the best precisions found in the literature for this mass range but do not rely on theoretical isochrones (e.g., J. D. Hartman et al. 2019). In addition, the precisions are improved by a factor of $2\text{--}3$ over the recent measurements of WASP-121A,b from V. Bourrier et al. (2020). We report these values in Table 2 and include updated related parameters.

4.2. Stellar Evolution Modeling

We derive the fundamental and photospheric stellar parameters of WASP-121 using the `isochrones` (T. D. Morton 2015) package to execute with `MultiNest` (F. Feroz & M. P. Hobson 2008; F. Feroz et al. 2009, 2019) a simultaneous Bayesian fit of the MESA Isochrones & Stellar Tracks (MIST) isochrone grid (B. Paxton et al. 2011, 2013; J. Choi et al. 2016; A. Dotter 2016; B. Paxton et al. 2018, 2019; A. S. Jermyn et al. 2023) to a curated collection of data for the star given in Table 1. We fit the MIST grid to (1) SkyMapper Southern Survey DR4 *uvgr* photometry including in quadrature its zero-point uncertainties (0.03, 0.02, 0.01, 0.01, 0.01) mag (C. A. Onken et al. 2024), Gaia DR2 *G* photometry including in quadrature its zero-point uncertainty (Gaia Collaboration et al. 2016; F. Arenou et al. 2018; G. Busso et al. 2018; D. W. Evans et al. 2018; Gaia Collaboration et al. 2018; M. Riello et al. 2018), Two Micron All Sky Survey (2MASS)

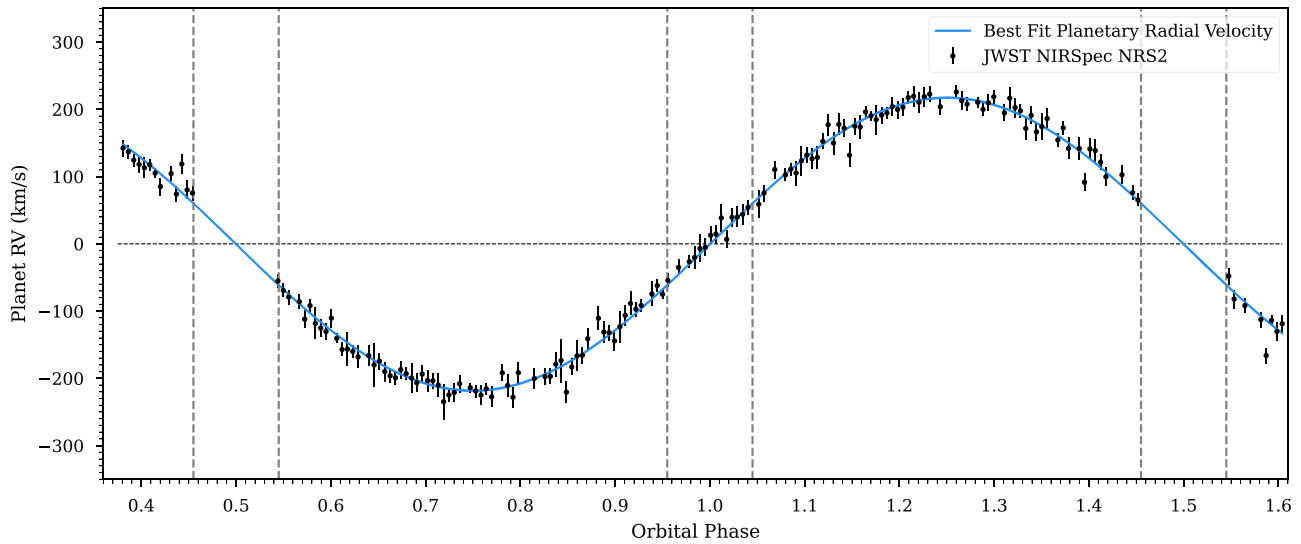


Figure 6. The planetary RV signal derived using NIRSpec/NRS2 with 1σ uncertainties (black data points). A best-fit planetary RV signal is also shown (blue) as well as the eclipse and transit first and fourth contact phases (gray dashed lines). The RV data are available as the data behind the figure.

(The data used to create this figure are available in the [online article](#).)

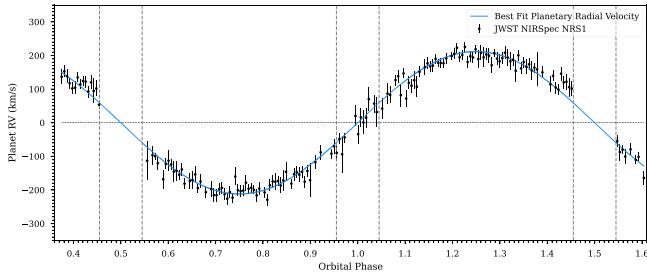


Figure 7. Same as Figure 6 but for NIRSpec/NRS1. The RV data are available as the data behind the figure.

(The data used to create this figure are available in the [online article](#).)

Table 1
WASP-121A Isochrone Inputs

Parameter	Value
SkyMapper u	11.7994 ± 0.0230
SkyMapper v	11.3884 ± 0.0200
SkyMapper g	10.5448 ± 0.0146
SkyMapper r	10.3774 ± 0.0149
SkyMapper i	10.3499 ± 0.0151
Gaia G DR2	10.3746 ± 0.01
2MASS J	9.625 ± 0.021
2MASS H	9.439 ± 0.025
2MASS K_s	9.374 ± 0.022
WISE W1	9.365 ± 0.033
WISE W2	9.387 ± 0.038
WISE W3	9.383 ± 0.062
Parallax (mas)	3.8114 ± 0.0135
A_v	0.1118 ± 0.0013

JHK_s photometry including its zero-point uncertainties (M. F. Skrutskie et al. 2006), and Wide-field Infrared Survey Explorer CatWISE2020 W1W2W3 photometry including in quadrature its zero-point uncertainties (0.032, 0.037, 0.051) mag (E. L. Wright et al. 2010; A. Mainzer et al. 2011; F. Marocco et al. 2021); (2) a zero-point-corrected Gaia DR3 parallax (C. Fabricius et al. 2021; Gaia Collaboration et al. 2021; L. Lindgren et al. 2021a, 2021b; N. Rowell et al. 2021;

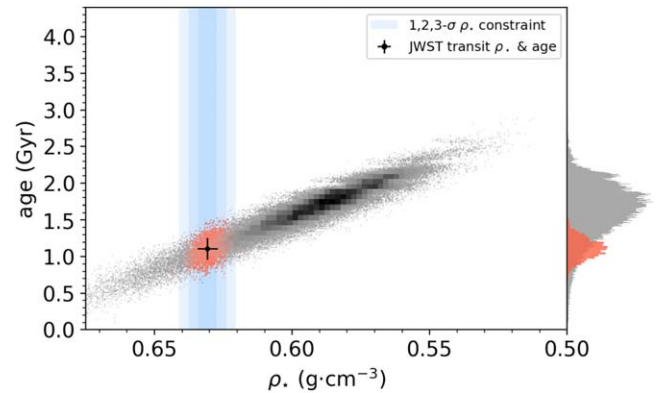


Figure 8. Isochrone posterior values of the age vs. stellar density considering only the broadband magnitudes, parallax, and extinction (gray/black). An updated posterior with the added constraint of the JWST stellar density is also shown (red). The JWST-measured stellar density and isochrone age are indicated with the black data point, with 1, 2, and 3σ density confidence intervals shown (blue).

F. Torra et al. 2021) with the formal uncertainty increased by 30% (K. El-Badry et al. 2021); and (3) an estimated reddening value based on a three-dimensional reddening map (R. Lalle et al. 2022; J. L. Vergely et al. 2022). For the GAIA photometry, we increased the error bar of the reported G -band photometry by 0.01 mag, which takes into account the observed epoch-to-epoch scatter of the GAIA photometry, which we postulate as due to stellar activity. We use a log uniform age prior between 0.1 and 10 Gyr, a uniform extinction prior in the interval $0 \text{ mag} < A_v < 0.2 \text{ mag}$, and a distance prior proportional to volume between the C. A. L. Bailer-Jones et al. (2021) geometric distance minus/plus 5 times its uncertainty. The modeling is also constrained by a precise scaled semimajor axis value (a/R_s) derived from the JWST transit light curve (C. Gapp et al. 2024, private communication), which provides tight constraints on the stellar density.

The results are shown in Figures 8 and 9 with the derived values in Table 2. We derive an age of 1.11 ± 0.14 Gyr for the system. Our age is consistent with previous estimates (F. Borsa et al. 2021), though $3\times$ more precise given the added constraint

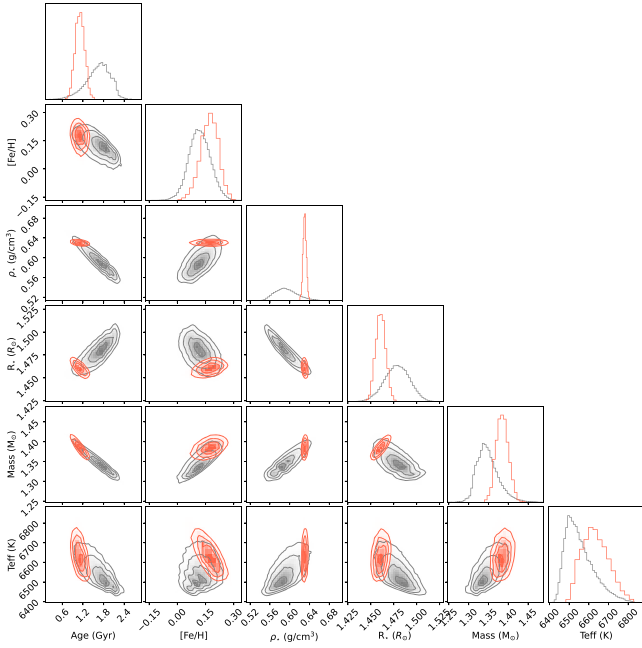


Figure 9. Isochrones posterior distribution of stellar parameters (gray/black) along with the posterior constrained with the JWST transit-measured stellar density (red), with the values listed in Table 2.

of the JWST transit-measured stellar density. We also compare the isochrone-derived mass to the dynamical mass in Figure 10, finding good agreement.

5. Results

5.1. Tidally Mediated Orbital Evolution

Unlike most hot Jupiter systems, the orbital period of the WASP-121 system at $P = 1.27492504 \pm 0.000000145$ days is longer than the rotation period of the star WASP-121 at $P_{\text{rot}} \approx 1.13$ days (L. Delrez et al. 2016). As a consequence, if WASP-121’s stellar obliquity ψ was identically zero, then angular momentum would move from stellar rotation to the orbit of the star–planet system, thereby increasing its orbital period and semimajor axis. WASP-121 has stellar obliquity $\psi = 88^\circ.1$ though (V. Bourrier et al. 2020), necessitating a more comprehensive treatment of the system’s tidal evolution. We therefore use the tidal evolution model outlined in J. Leconte et al. (2010) to predict the instantaneous change in WASP-121’s orbital period due to star–planet tidal interactions. Using (1) a , M_* , R_* , M_p , and R_p reported in Table 2; (2) $P_{\text{rot}} = 1.13$ days from L. Delrez et al. (2016); (3) $\psi = 88^\circ.1$ from V. Bourrier et al. (2020); (4) a stellar moment of inertia $I/M_*R_*^2 = 0.056$ based on models presented in L. Amard et al. (2019) for the evolution of rotating stars; and (5) assuming $e = 0$ and modified planetary tidal quality factor $Q'_p = 10^5$ as appropriate for a giant planet, we can predict \dot{P} for the WASP-121 system as a function of modified stellar tidal quality factor Q'_* .

We find $\dot{P} = -8.5 \times 10^{-6} (10^8/Q'_*) \text{ s yr}^{-1}$. Even if WASP-121 is highly dissipative like WASP-12 with $Q'_* \sim 10^5$, then $\dot{P} = -8.5 \text{ ms yr}^{-1}$, a factor of about 3 less than the \dot{P} observed in the WASP-12 system (e.g., S. W. Yee et al. 2020). While the value of Q'_* for WASP-121 is uncertain, N. N. Weinberg et al. (2024) calculated Q'_* as a function of stellar mass, stellar age, system orbital period, and planet mass. For systems like

WASP-121, they predict $Q'_* \sim 10^8$, which implies a vanishingly small and certainly undetectable $\dot{P} = -8.5 \mu\text{s yr}^{-1}$.

5.2. Planetary Wind Constraints

We find a tentative $\Delta K_{\text{NRS2-NRS1}} = 5.5 \pm 2.2 \text{ km s}^{-1}$ difference in the RV measurement between the NRS1 and NRS2 detectors (2.5σ confidence). In particular, the measured velocity of NRS1 at $212.7 \pm 1.8 \text{ km s}^{-1}$ is slower than the expected planetary orbital velocity of $217.8 \pm 1.0 \text{ km s}^{-1}$ (calculated using Equation (1) with the updated values from Table 2).

Unlike RV measurements of the star, the tidally locked planet has large day/night temperature differences, which can affect the measurements. In the absence of such differences, the velocity shifts imparted from the rotation of the planet and global equatorial winds will largely cancel out. With strong day/night differences, the planet can induce RV signals beyond the orbital velocity itself. For instance, in a limiting case where the nightside flux is negligible and the planetary emission emanates entirely from the hot dayside, the tidally locked rotation and equatorial winds will both act to reduce the measured RV (see Figure 11).

We performed an analytical estimate to better quantify the contributions from winds and the planet rotation on the NRS1/NRS2 velocity difference, concentrating first on relative velocity differences. We estimated the values at quadrature, given that phase has the maximum velocity signature and the planet can easily be divided geometrically into equal dayside and nightside components. With a 5.5 km s^{-1} difference observed between the detectors, we estimated what fraction of that difference could be directly attributable to the planet’s rotation. At the equator, we calculate a planetary rotational velocity of $K_{\text{rot}} = 7.6 \text{ km s}^{-1}$ derived from the planet’s radius and orbital period (assuming the planet is tidally locked). As the bulk of planetary flux will be emitted from the equatorial region, which is expected to be hottest (N. J. Mayne et al. 2014; V. Parmentier et al. 2018; E. K. H. Lee et al. 2022), we estimated the rotational velocity components along the equator at the average angle emitted from the planet ($\mu = \cos(\theta) = 1/2$) or $\theta = 60^\circ$. We flux-weighted the dayside and nightside contributions, F_d and $F_n = 1 - F_d$, respectively, from the bulk planetary rotation, taking the projected $\sin(\theta)$ component contributing to the measured Doppler shifts, giving

$$\Delta K_{\text{rot}} = (1 - F_d)K_{\text{rot}} \sin(\theta) + F_d K_{\text{rot}} \sin(\theta). \quad (3)$$

For NRS1, $F_d = 96\%$, as measured by T. Mikal-Evans et al. (2023), giving an estimated RV shift of 6.0 km s^{-1} , while $F_d = 88\%$ for NRS2, giving an estimated RV shift of 5.0 km s^{-1} . Thus, the RV difference between the two detectors that can be attributable to the planetary rotation should be 1 km s^{-1} . This implies that the wind speed difference between the pressures probed between the two detectors is $4.5 \pm 2.2 \text{ km s}^{-1}$. These estimates are in line with current predictions (E. K. H. Lee et al. 2022), which find speeds up to 8 km s^{-1} and large vertical differences in wind speeds.

The NRS1 and NRS2 detectors are expected to probe different pressure levels, as the chemical and thermal differences from equator to pole and from the dayside to nightside mean that at constant wavelength the pressure and height in the atmosphere one is detecting at a given optical depth varies. NRS1 is expected to be sensitive to H_2O in

Table 2
System Parameters for WASP-121A,b

Parameter	Description	Units	Value	Reference(s)
Measured planet parameters				
K_p	RV semiamplitude	km s^{-1}	215.7 ± 1.1	this work
P	orbital period	days	$1.27492504 \pm 0.00000015$	V. Bourrier et al. (2020)
a/R_*	scaled semimajor axis	...	3.7844 ± 0.0069	C. Gapp et al. (2024, private communication)
R_p/R_*	planet–star radius ratio	...	0.122551 ± 0.000063	T. Mikal-Evans et al. (2023)
$(R_p/R_*)^2$	transit depth	...	0.015018 ± 0.000015	T. Mikal-Evans et al. (2023)
Measured stellar parameters				
K_*	RV semiamplitude	m s^{-1}	181.1 ± 6.4	L. Delrez et al. (2016)
ρ_*	stellar density	g cm^{-3}	0.6308 ± 0.0034	this work
d	distance	pc	263.18 ± 0.72	Gaia Collaboration et al. (2023)
Inferred planet parameters				
T_{eq}	equilibrium temperature	K	2409 ± 24	this work
a	semimajor axis	au	0.02571 ± 0.00010	this work
R_p	planet radius	R_J	1.7420 ± 0.0060	this work
ρ_p	planetary density	g cm^{-3}	0.275 ± 0.010	this work
Dynamically determined parameters				
M_p	planet mass	M_J	1.170 ± 0.043	this work
M_*	stellar mass	M_\odot	1.330 ± 0.019	this work
Inferred isochrones stellar parameters				
M_*	stellar mass	M_\odot	1.385 ± 0.016	this work
R_*	stellar radius	R_\odot	1.461 ± 0.005	this work
$\log(g)$	surface gravity	$\log_{10}(\text{cm s}^{-2})$	4.251 ± 0.003	this work
T_{eff}	effective temperature	K	6628 ± 66	this work
[Fe/H]	metallicity	$\log([\text{Fe}/\text{H}]_\odot)$	0.17 ± 0.05	this work
τ_{iso}	isochronal age	$\times 10^9 \text{ yr}$	1.11 ± 0.14	this work

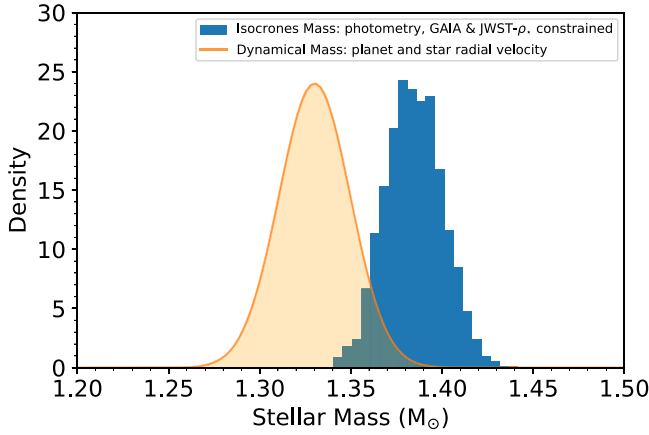


Figure 10. Dynamic RV stellar mass measurement compared to the stellar modeling mass constrained by the broadband photometry, distance, and stellar density.

particular, while NRS2 at longer wavelengths is sensitive to strong CO and CO₂ lines (e.g., Z. Rustamkulov et al. 2022). These pressure and longitude differences can result in differing wind profiles. Comparing the absolute velocities measured, the velocity from NRS2 of $218.2 \pm 1.0 \text{ km s}^{-1}$ matches the expected velocity of $217.8 \pm 1.0 \text{ km s}^{-1}$ calculated using the JWST transit-derived a/R_* and R_* constrained using GAIA. With a $\sim 5 \text{ km s}^{-1}$ shift expected from the planet’s rotation not observed, this implies a counterrotating wind component is largely able to cancel out this expected shift. The wind patterns from general circulation modeling (GCM) predict that such counterrotating winds contribute at high latitudes (E. K. H. Lee et al. 2022). The lower RV value inferred from the NRS1 observations, relative to NRS2, suggests either that the prograde wind (i.e., flowing in the direction of the planet’s

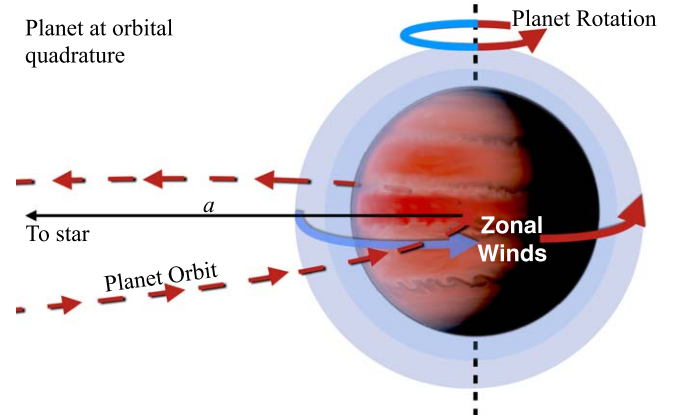


Figure 11. Illustration of the planet at orbital quadrature (phase 1.25) and the red/blueshifted velocity and day/night components. At this phase, the planet is redshifted from the orbital velocity, the dayside emission of the planet is blueshifted from winds and rotation, while the fainter nightside is redshifted from winds and rotation.

rotation) contributes more substantially to the signal or that the wind speeds at high latitudes are slower. Deprojected, the nonrotational 4.5 km s^{-1} RV difference suggests zonal wind speeds on the order of $4.5/\sin(\theta) = 5.2 \text{ km s}^{-1}$.

A more sophisticated three-dimensional treatment that takes into account the full viewing geometry, temperature structure, and atmospheric composition will be needed to interpret the winds using this technique. However, this estimate indicates that the winds can be probed with JWST phase-curve emission data given the sensitivity to the Doppler shifts from the global planetary emission lines. Further, isolating and comparing specific spectral lines from the emission spectra (e.g., CO versus H₂O) can lead to further insights; however, such studies are beyond the scope of this work.

These measurements nicely complement the existing high-resolution optical transit and phase-curve measurements (e.g., H. J. Hoeijmakers et al. 2024; C. Maguire et al. 2023) that probe higher altitudes in atomic transitions. In particular, several species including Fe have been detected at near-ultraviolet and optical wavelengths and at altitudes beyond the Roche limit (D. K. Sing et al. 2019; C. Maguire et al. 2023). The phase-curve measurements here are probing molecular emission near the mbar to bar region, which can give insight into the large equatorial jets expected on these planets. As the GCM wind speeds are highly dependent on the modeled diffusion (C. S. Cooper & A.P. Showman 2005; N. J. Mayne et al. 2014), comparing the theoretical wind speed values to the observations should help calibrate these types of models. The large wind speeds estimated here are an indication the equatorial jets can be driven to high velocities in ultrahot Jupiters. We note that the significance (2.4σ) is similar to that of the first wind speed measurement from CO on HD 209458b (I. A. G. Snellen et al. 2008). Given the potential differences between species (e.g., J. P. Wardenier et al. 2024), these estimates may be further refined by studies isolating specific molecular features and further emission/transmission spectral measurements, which will improve the atmospheric constraints and therefore the correlation with model atmospheres.

6. Conclusion

We have presented an RV measurement for the planet WASP-121b, which we detected during the entire orbital phase using JWST NIRSpec. Such measurements require the high-resolution gratings of NIRSpec, which are capable of detecting the orbital motion of close-in planets during phase-curve observations.

With NIRSpec, we measured the RV of the planet to 0.5% precision, with $K_p = 215.7 \pm 1.1 \text{ km s}^{-1}$. This is the first time an exoplanet's RV has been continuously measured during an entire orbit. With both the star and planet semi-amplitude RV detected, the absolute masses of both components were precisely determined. We found that WASP-121A has a mass of $M_* = 1.330 \pm 0.019 M_\odot$, while WASP-121b has a mass of $M_p = 1.170 \pm 0.043 M_{\text{Jup}}$. These masses are 2–3 times more precise than previous estimates and do not rely on stellar evolution models.

In the case of WASP-121b our radial velocities measure the mass of the star to 1.4%, the JWST transit measures the stellar density to 0.5%, and GAIA parallax and photometry measure the radius to 0.35%. All of these precise independent stellar measurements are consistent at the 1σ level. As a result, the planetary mass and radius parameters are also precise and can be derived free of stellar modeling. Our 1.4% stellar mass uncertainty improves upon the $\sim 5\%$ inherent uncertainty from estimating stellar masses using stellar models (J. Tayar et al. 2022), with our data providing valuable calibration information. In the case of WASP-121A, the good match to the stellar evolution models indicates the MESA models are accurate for this stellar type. This assessment agrees with results benchmarking the models to an open cluster (W. Brandner et al. 2023). There are a number of targets where these measurements can be made, as a number of planets have either comparable or higher-emission spectral signals or higher-amplitude planetary radial velocities (e.g., TOI-2109 b expected to be 291 km s^{-1}).

Using stellar evolution models constrained with a precise JWST stellar density derived from the NIRSpec transit light

curve, we found that the system is $1.11 \pm 0.14 \text{ Gyr}$ old. This age makes the star only in the first quarter of its main-sequence lifetime. Our JWST planetary RV measurements on a $K = 9.3 \text{ mag}$ star were able to reach median precisions of 11 km s^{-1} in a 11.25 minute observation and 1 km s^{-1} for the whole 1.57 day phase curve. Future observers should consider phase-curve measurements with the high-resolution NIRSpec, as precision absolute masses can be obtained for both the star and planet independent of stellar evolution models, and constraining the zonal winds appears feasible. The large shifts in the planetary signal (~ 10 pixels) also highlights that the planetary RV will have to be taken into account when retrieving the atmospheric properties from the whole phase-curve signal. Otherwise, key molecular lines will not align in wavelength with the model.

Finally, we observed a potential wavelength dependence to the RV amplitude, with the shorter wavelength NRS1 detector lower by $5.5 \pm 2.2 \text{ km s}^{-1}$. We estimated that the planet's rotation can account for only 1 km s^{-1} of the difference, with $4.5 \pm 2.2 \text{ km s}^{-1}$ attributable to average zonal wind speeds tentatively estimated to be about 5.2 km s^{-1} .

Acknowledgments

This work is based on observations made with the NASA/ESA/CSA James Webb Space Telescope. The data were obtained from the Mikulski Archive for Space Telescopes at the Space Telescope Science Institute, which is operated by the Association of Universities for Research in Astronomy, Inc., under NASA contract NAS 5-03127 for JWST. These observations are associated with program 1729. The data presented in this article were obtained from the Mikulski Archive for Space Telescopes (MAST) at the Space Telescope Science Institute. The specific observations analyzed can be accessed via doi:[10.17909/6qnn-6j23](https://doi.org/10.17909/6qnn-6j23). Support for JWST program GO-1729 was provided by NASA through a grant from the Space Telescope Science Institute, which is operated by the Association of Universities for Research in Astronomy, Inc., under NASA contract NAS 5-26555. J.K.B. was supported by a Science and Technology Facilities Council Ernest Rutherford Fellowship. N.J.M. acknowledges support from a UKRI Future Leaders Fellowship [Grant MR/T040866/1], a Science and Technology Facilities Funding Council Nucleus Award [Grant ST/T000082/1], and the Leverhulme Trust through a research project grant [RPG-2020-82]. N.M. was partly supported by a Science and Technology Facilities Council Consolidated Grant [ST/R000395/1], the Leverhulme Trust through a research project grant [RPG2020-82], and a UKRI Future Leaders Fellowship [grant No. MR/T040866/1]. This work has made use of data from the European Space Agency (ESA) mission Gaia (<https://www.cosmos.esa.int/gaia>), processed by the Gaia Data Processing and Analysis Consortium (DPAC; <https://www.cosmos.esa.int/web/gaia/dpac/consortium>). Funding for the DPAC has been provided by national institutions, in particular the institutions participating in the Gaia Multilateral Agreement.

Data Availability

The RV data products as shown in Figures 6 and 7 are available on Zenodo at doi:[10.5281/zenodo.11992282](https://doi.org/10.5281/zenodo.11992282).

Facility: JWST(NIRSpec).

Software: NumPy (T. Oliphant 2006), SciPy (P. Virtanen et al. 2019), Matplotlib (T. A. Caswell et al. 2019), AstroPy (Astropy Collaboration et al. 2018).

ORCID iDs

David K. Sing  <https://orcid.org/0000-0001-6050-7645>

Thomas M. Evans-Soma  <https://orcid.org/0000-0001-5442-1300>

Zafar Rustamkulov  <https://orcid.org/0000-0003-4408-0463>

Joshua D. Lothringer  <https://orcid.org/0000-0003-3667-8633>

Nathan J. Mayne  <https://orcid.org/0000-0001-6707-4563>

Kevin C. Schlaufman  <https://orcid.org/0000-0001-5761-6779>

References

- Alderson, L., Wakeford, H. R., Alam, M. K., et al. 2023, *Natur*, 614, 664
- Amard, L., Palacios, A., Charbonnel, C., et al. 2019, *A&A*, 631, A77
- Arenou, F., Luri, X., Babusiaux, C., et al. 2018, *A&A*, 616, A17
- Astropy Collaboration, Price-Whelan, A. M., Sipőcz, B. M., et al. 2018, *AJ*, 156, 123
- August, P. C., Bean, J. L., Zhang, M., et al. 2023, *ApJL*, 953, L24
- Azevedo Silva, T., Demangeon, O. D. S., Santos, N. C., et al. 2022, *A&A*, 666, L10
- Bailer-Jones, C. A. L., Rybizki, J., Fousneau, M., Demleitner, M., & Andrae, R. 2021, *AJ*, 161, 147
- Bean, J. L., Xue, Q., August, P. C., et al. 2023, *Natur*, 618, 43
- Bell, T. J., Crouzet, N., Cubillos, P. E., et al. 2024, *NatAs*, 8, 879
- Ben-Yami, M., Madhusudhan, N., Cabot, S. H. C., et al. 2020, *ApJL*, 897, L5
- Birkby, J. L. 2018, in *Handbook of Exoplanets*, ed. H. J. Deeg & J. A. Belmonte (Berlin: Springer), 16
- Birkby, J. L., de Kok, R. J., Brogi, M., Schwarz, H., & Snellen, I. A. G. 2017, *AJ*, 153, 138
- Böker, T., Beck, T. L., Birkmann, S. M., et al. 2023, *PASP*, 135, 038001
- Borsa, F., Allart, R., Casasayas-Barris, N., et al. 2021, *A&A*, 645, A24
- Bourrier, V., Ehrenreich, D., Lendl, M., et al. 2020, *A&A*, 635, A205
- Brandner, W., Calissendorff, P., & Kopytova, T. 2023, *MNRAS*, 518, 662
- Busso, G., Cacciari, C., Carrasco, J. M., et al. 2018, Gaia DR2 Documentation 5, European Space Agency
- Cabot, S. H. C., Madhusudhan, N., Welbanks, L., Piette, A., & Gandhi, S. 2020, *MNRAS*, 494, 363
- Caswell, T. A., Droettboom, M., Hunter, J., et al. 2019, *matplotlib/matplotlib* v3.1.0, Zenodo, doi:10.5281/zenodo.2893252
- Choi, J., Dotter, A., Conroy, C., et al. 2016, *ApJ*, 823, 102
- Cooper, C. S., & Showman, A. P. 2005, *ApJL*, 629, L45
- Coulombe, L.-P., Benneke, B., Challener, R., et al. 2023, *Natur*, 620, 292
- Delrez, L., Santerne, A., Almenara, J.-M., et al. 2016, *MNRAS*, 458, 4025
- Dotter, A. 2016, *ApJS*, 222, 8
- El-Badry, K., Rix, H.-W., & Heintz, T. M. 2021, *MNRAS*, 506, 2269
- Esparza-Borges, E., López-Morales, M., Adams Redai, J. I., et al. 2023, *ApJL*, 955, L19
- Espinoza, N., Úbeda, L., Birkmann, S. M., et al. 2023, *PASP*, 135, 018002
- Evans, D. W., Riello, M., De Angeli, F., et al. 2018, *A&A*, 616, A4
- Evans, T. M., Sing, D. K., Goyal, J. M., et al. 2018, *AJ*, 156, 283
- Evans, T. M., Sing, D. K., Kataria, T., et al. 2017, *Natur*, 548, 58
- Evans, T. M., Sing, D. K., Wakeford, H. R., et al. 2016, *ApJL*, 822, L4
- Fabricsius, C., Luri, X., Arenou, F., et al. 2021, *A&A*, 649, A5
- Feroz, F., & Hobson, M. P. 2008, *MNRAS*, 384, 449
- Feroz, F., Hobson, M. P., & Bridges, M. 2009, *MNRAS*, 398, 1601
- Feroz, F., Hobson, M. P., Cameron, E., & Pettitt, A. N. 2019, *OJAp*, 2, 10
- Gaia Collaboration, Brown, A. G. A., Vallenari, A., et al. 2018, *A&A*, 616, A1
- Gaia Collaboration, Brown, A. G. A., Vallenari, A., et al. 2021, *A&A*, 649, A1
- Gaia Collaboration, Prusti, T., de Bruijne, J. H. J., et al. 2016, *A&A*, 595, A1
- Gaia Collaboration, Vallenari, A., Brown, A. G. A., et al. 2023, *A&A*, 674, A1
- Gibson, N. P., Merritt, S., Nugroho, S. K., et al. 2020, *MNRAS*, 493, 2215
- Grant, D., Lothringer, J. D., Wakeford, H. R., et al. 2023, *ApJL*, 949, L15
- Hartman, J. D., Bakos, G. Á, Bayliss, D., et al. 2019, *AJ*, 157, 55
- Hellier, C., Anderson, D. R., Barakaoui, K., et al. 2019, *MNRAS*, 490, 1479
- Hoeijmakers, H. J., Kitzmann, D., Morris, B. M., et al. 2024, *A&A*, 685, A139
- Jermyn, A. S., Bauer, E. B., Schwab, J., et al. 2023, *ApJS*, 265, 15
- JWST Transiting Exoplanet Community Early Release Science Team, Ahrer, E. M., Alderson, L., et al. 2023, *Natur*, 614, 649
- Lallement, R., Vergely, J. L., Babusiaux, C., & Cox, N. L. J. 2022, *A&A*, 661, A147
- Lecote, J., Chabrier, G., Baraffe, I., & Levrard, B. 2010, *A&A*, 516, A64
- Lee, E. K. H., Prinoth, B., Kitzmann, D., et al. 2022, *MNRAS*, 517, 240
- Lindgren, L., Bastian, U., Biermann, M., et al. 2021a, *A&A*, 649, A4
- Lindgren, L., Klioner, S. A., Hernández, J., et al. 2021b, *A&A*, 649, A2
- Lothringer, J. D., Barman, T., & Koskinen, T. 2018, *ApJ*, 866, 27
- Lustig-Yaeger, J., Fu, G., May, E. M., et al. 2023, *NatAs*, 7, 1317
- Maguire, C., Gibson, N. P., Nugroho, S. K., et al. 2023, *MNRAS*, 519, 1030
- Mainzer, A., Bauer, J., Grav, T., et al. 2011, *ApJ*, 731, 53
- Marocco, F., Eisenhardt, P. R. M., Fowler, J. W., et al. 2021, *ApJS*, 253, 8
- Mayne, N. J., Baraffe, I., Acreman, D. M., et al. 2014, *A&A*, 561, A1
- Merritt, S. R., Gibson, N. P., Nugroho, S. K., et al. 2021, *MNRAS*, 506, 3853
- Mikal-Evans, T., Sing, D. K., Dong, J., et al. 2023, *ApJL*, 943, L17
- Mikal-Evans, T., Sing, D. K., Goyal, J. M., et al. 2019, *MNRAS*, 488, 2222
- Miles, B. E., Biller, B. A., Patapis, P., et al. 2023, *ApJL*, 946, L6
- Morton, T. D. 2015, *isochrones: Stellar Model Grid Package*, Astrophysics Source Code Library, ascl:1503.010
- Oliphant, T. 2006, *NumPy: A Guide to NumPy* (USA: Trelgol Publishing)
- Onken, C. A., Wolf, C., Bessell, M. S., et al. 2024, *PASA*, 41, e061
- Parmentier, V., Line, M. R., Bean, J. L., et al. 2018, *A&A*, 617, A110
- Paxton, B., Bildsten, L., Dotter, A., et al. 2011, *ApJS*, 192, 3
- Paxton, B., Cantiello, M., Arras, P., et al. 2013, *ApJS*, 208, 4
- Paxton, B., Schwab, J., Bauer, E. B., et al. 2018, *ApJS*, 234, 34
- Paxton, B., Smolec, R., Schwab, J., et al. 2019, *ApJS*, 243, 10
- Ridden-Harper, A., de Mooij, E., Jayawardhana, R., et al. 2023, *AJ*, 165, 211
- Riello, M., De Angeli, F., Evans, D. W., et al. 2018, *A&A*, 616, A3
- Rigby, J., Perrin, M., McElwain, M., et al. 2023, *PASP*, 135, 048001
- Rowell, N., Davidson, M., Lindgren, L., et al. 2021, *A&A*, 649, A11
- Rustamkulov, Z., Sing, D. K., Liu, R., & Wang, A. 2022, *ApJL*, 928, L7
- Rustamkulov, Z., Sing, D. K., Mukherjee, S., et al. 2023, *Natur*, 614, 659
- Seidel, J. V., Borsa, F., Pino, L., et al. 2023, *A&A*, 673, A125
- Sing, D. K., Holberg, J. B., Burleigh, M. R., et al. 2004, *AJ*, 127, 2936
- Sing, D. K., Lavvas, P., Ballester, G. E., et al. 2019, *AJ*, 158, 91
- Skrutskie, M. F., Cutri, R. M., Stiening, R., et al. 2006, *AJ*, 131, 1163
- Snellen, I. A. G., Albrecht, S., de Mooij, E. J. W., & Le Poole, R. S. 2008, *A&A*, 487, 357
- Snellen, I. A. G., de Kok, R. J., de Mooij, E. J. W., & Albrecht, S. 2010, *Natur*, 465, 1049
- Tayar, J., Claytor, Z. R., Huber, D., & van Saders, J. 2022, *ApJ*, 927, 31
- Torra, F., Castañeda, J., Fabricius, C., et al. 2021, *A&A*, 649, A10
- Torres, G., Andersen, J., & Giménez, A. 2010, *A&ARv*, 18, 67
- van Sluijs, L., Birkby, J. L., Lothringer, J., et al. 2023, *MNRAS*, 522, 2145
- Vergely, J. L., Lallement, R., & Cox, N. L. J. 2022, *A&A*, 664, A174
- Virtanen, P., Gommers, R., Burovski, E., et al. 2019, *scipy/scipy: SciPy* v1.2.1, Zenodo, doi:10.5281/zenodo.2560881
- Wardenier, J. P., Parmentier, V., Line, M. R., et al. 2024, *PASP*, 136, 084403
- Weinberg, N. N., Davachi, N., Essick, R., et al. 2024, *ApJ*, 960, 50
- Wright, E. L., Eisenhardt, P. R. M., Mainzer, A. K., et al. 2010, *AJ*, 140, 1868
- Yee, S. W., Winn, J. N., Hartman, J. D., et al. 2023, *ApJS*, 265, 1
- Yee, S. W., Winn, J. N., Knutson, H. A., et al. 2020, *ApJL*, 888, L5